Ab initio study of the magnetostructural properties of MnAs

Ivan Rungger and Stefano Sanvito
School of Physics, Trinity College, Dublin 2, Ireland
(Received 24 January 2006; revised manuscript received 12 May 2006; published 31 July 2006)

The magnetic and structural properties of MnAs are studied with *ab initio* methods and by mapping total energies onto a Heisenberg model. The stability of the different phases is found to depend mainly on the volume and on the amount of magnetic order, confirming previous experimental findings and phenomenological models. It is generally found that for large lattice constants the ferromagnetic state is favored, whereas for small lattice constants different antiferromagnetic states can be stabilized. In the ferromagnetic state the structure with minimal energy is always hexagonal, whereas it becomes orthorhombically distorted if there is an antiferromagnetic alignment of the magnetic moments in the hexagonal plane. For the paramagnetic state the stable cell is found to be orthorhombic up to a critical lattice constant of about 3.7 Å, above which it remains hexagonal. This leads to the second-order structural phase transition between paramagnetic states at about 400 K, where the lattice parameter increases above this critical value with rising temperature due to the thermal expansion. We also evaluate the magnetic susceptibility as a function of temperature, from which a semiquantitative description of the MnAs phase diagram emerges.

DOI: 10.1103/PhysRevB.74.024429 PACS number(s): 75.80.+q, 64.70.−p, 71.70.Gm

I. INTRODUCTION

MnAs is an extremely promising material for magnetoelectronics, since it can grow epitaxially on GaAs (Ref. 1) and Si (Ref. 2), forming clean and atomically sharp interfaces.[2] MnAs/GaAs heterojunctions have been extensively studied experimentally,[1,3–5] and spin injection from MnAs into GaAs has been demonstrated.[6] However, one of the major drawbacks for the use of MnAs in devices is the fact that bulk MnAs has a phase transition at 318 K, where the magnetic state changes from ferromagnetic to paramagnetic. Moreover, when grown on GaAs, this temperature changes depending on the growth direction. This is mainly attributed to the induced strain.[1,3,7,8] The aim of this paper is to use *ab initio* density functional theory (DFT) calculations to develop an understanding of the phase transitions of MnAs, which can be compared with experiments and with existing phenomenological models.

First a review of the experimental properties of MnAs is presented and a brief description of the existing phenomenological models is given. Then the results of our *ab initio* calculations are presented and compared to experiments and models. Within the scope of a Heisenberg model the exchange coupling constants are calculated for different distorted unit cells, and the Curie temperature and its dependence on the lattice parameters are evaluated in the mean-field approximation. We also predict the ground-state volume and lattice structure for the paramagnetic state, demonstrating that the phase transitions of MnAs can indeed be explained by *ab initio* calculations. Finally a simple model for the susceptibility as function of temperature is given and a qualitative description of the phase diagram of MnAs will emerge.

II. EXPERIMENTAL PROPERTIES AND EXISTING MODELS

MnAs is a ferromagnetic metal at low temperature but it becomes paramagnetic at T_p=318 K, when the magnetic moment abruptly vanishes (Fig. 1), the resistivity increases discontinuously,[9] the volume is reduced by 2.1%, and the lattice structure changes from hexagonal $B8_1$ (NiAs type) to orthorhombic $B31$ (MnP type).[10–14] A latent heat of 7490 J/kg is associated with this transition.[11] Hysteresis is present with a phase transition temperature of 307 K upon cooling and of 318 K upon heating.[13] All these properties clearly indicate a first-order phase transition.

Above T_p the distortion reduces continuously, until it vanishes at $T_t \approx 398$ K,[10] where the crystal structure changes back to $B8_1$. There is no latent heat, but only a discontinuity in the heat capacity of the material; i.e., this phase transition is of second order. For temperatures between T_p and T_t the paramagnetic susceptibility has an anomalous behavior. It increases with increasing temperature until it reaches a maximum at T_t. Above T_t it decreases and has a Curie-Weiss behavior (Fig. 1). Moreover, at T_t there is a λ point in the specific heat.[15] Application of a magnetic field transforms the $B31$ structure back to $B8_1$ above a critical field.[9,16–19]

Figure 2 shows the phase diagram. If pressure is applied, T_p is lowered while T_t increases. Above the critical pressure

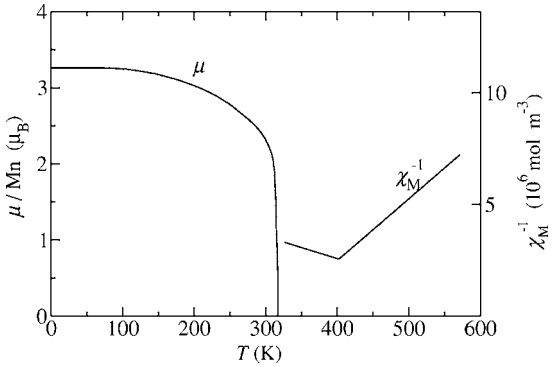

FIG. 1. Magnetization per Mn atom as a function of temperature for ferromagnetic MnAs below 318 K and inverse susceptibility for paramagnetic MnAs above 318 K as a function of temperature (schematically after Ref. 14).

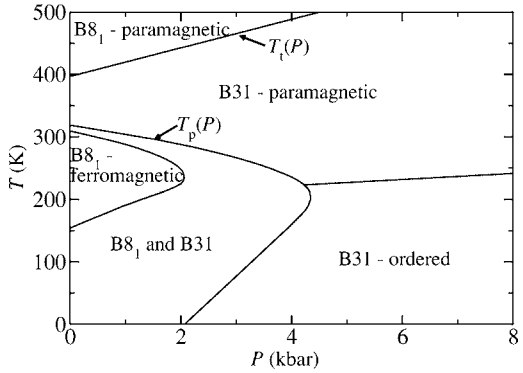

FIG. 2. Temperature (T) versus pressure (P) phase diagram of MnAs (adapted from Ref. 14), indicating also T_p and T_t as functions of pressure.

of 4.6 kbar the ferromagnetic $B8_1$ structure becomes unstable, and the material remains in the $B31$ structure for all temperatures below T_t. At high pressures and low temperatures different types of ordered magnetic structures are found, with a reduced saturation magnetic moment with respect to the zero-pressure ferromagnetic phase. Canted spin structures, similar to the helimagnetic structures of MnP,[20] are found at a pressure of 4.75 kbar below 210 K, with a local magnetic moment of about $3\mu_B$. A hysteresis region lies between the ferromagnetic and canted regions, where both states can be stabilized.

When the magnetic order breaks down and the system becomes paramagnetic, MnAs maintains the $B31$ structure for all pressures. As the temperature is further increased the structure of the cell continuously changes back towards $B8_1$, until at T_t it has again the $B8_1$ structure, with $\partial T_t/\partial P > 0$, where P is the pressure.

The magnetocrystalline anisotropy is quite strong in MnAs, with the c axis being the hard axis, so that the moments prefer to lie in the hexagonal plane.[12] Measurements of the magnetoelastic coupling[21] indicate that the coupling is stronger in the hexagonal plane than perpendicular to it.

Figure 3 shows the unit cells of MnAs in the hexagonal $B8_1$ and in the orthorhombic $B31$ crystal structures and it defines the unit cell vectors **a**, **b** ($\mathbf{b}_h$ for the $B8_1$ structure), and **c**. The $B8_1$ structure consists of stacked hexagonal layers of Mn and As atoms, and the unit cell contains two Mn and two As atoms. The $B31$ structure has twice the volume of $B8_1$ due to symmetry lowering and contains four Mn and four As atoms. The lattice is nearly hexagonal and the atoms are moved out of the hexagonal symmetry points along the **b** and **c** directions [Fig. 3(b)].

The Mn atoms are mainly displaced in the hexagonal plane along the **b** direction forming chains (Fig. 4), while the As atoms are displaced along the **c** axis. In each unit cell one of the planar As atoms is moved upwards and the other downwards with respect to the original position in the $B8_1$ structure, so as to keep the Mn-As distance nearly constant. The displacement u of the Mn atoms in the hexagonal plane lies between 0 and $0.05b$ ($b=|\mathbf{b}|$), depending on the temperature and pressure, and the displacement v of the As atoms along the c axis lies between 0 and $0.05c$ ($c=|\mathbf{c}|$). The $B8_1$ structure is a special case of the $B31$ structure, where $b=\sqrt{3}a$ and $u=v=0$. Therefore we choose the unit cell vectors in such a way that **a** and **c** have the same direction for both the $B8_1$ and $B31$ structures. In contrast the directions of the vectors $\mathbf{b}_h$ ($|\mathbf{b}_h|=|\mathbf{a}|=a$) for the hexagonal cell and **b** for the orthorhombic cell are different.

The lattice parameters of MnAs as a function of temperature[10,18,22,23] are shown in Fig. 5. They increase with temperature due to normal thermal expansion, although the in-plane parameter a decreases when the temperature gets near T_p and it jumps from 3.717 Å to 3.673 Å. The perpendicular parameter c increases continuously with temperature. At T_t there is an inflection in the slope of a and c as a function of temperature, and at about $T_s=450$ K (410 K in other measurements[23]) the slope changes discontinuously.

The exact temperature at which the distortion disappears is somewhat uncertain, and fluctuations may play a role for small distortions. The given temperature for the disappearing of the distortion corresponds to $T_t=398$ K.[10,23] However, measurements for small distortions are difficult and such a temperature can only be inferred. As pointed out in Ref. 24 the distortion should appear at temperatures slightly above T_t. Throughout this work we assume that the disappearing of the distortion occurs at T_s, which is the temperature where the thermal expansion coefficient of MnAs changes abruptly.

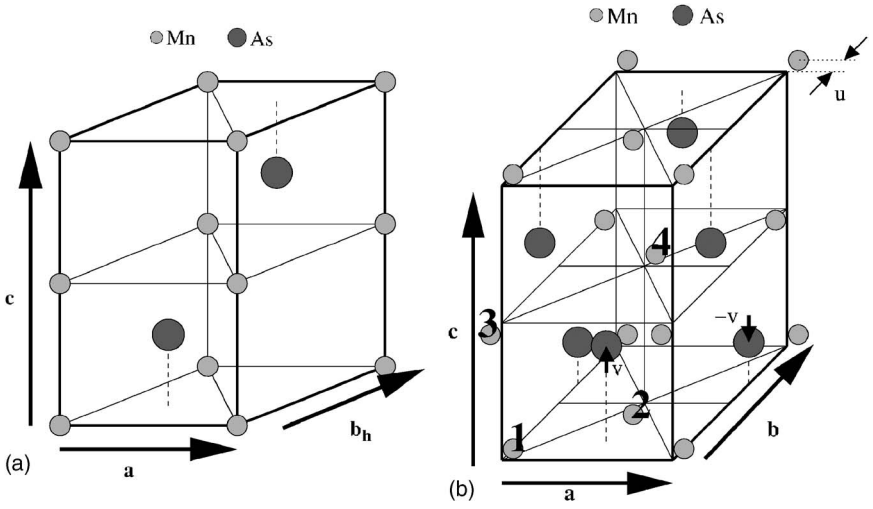

FIG. 3. (a) $B8_1$ unit cell containing two Mn and two As atoms, (b) $B31$ unit cell containing four Mn and four As atoms.

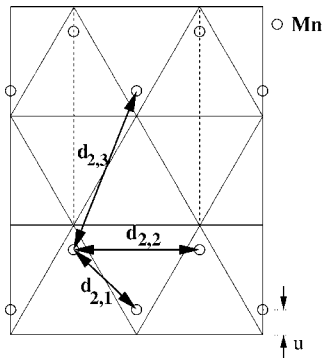

FIG. 4. Two-dimensional representation of one layer of Mn atoms in the $B31$ structure. d_{ij} represent the various Mn-Mn distances. The first index $i=2$ indicates that all the Mn are second nearest neighbors to each other in the $B8_1$ structure. The second index $j=1,2,3$ labels the three distances arising from the $B31$ distortion.

Early theories[25] believed that the phase transition at T_p was between ferromagnetic and antiferromagnetic order. This, however, was not supported by experiments[23] and led Bean and Rodbell (BR) to propose a model where the exchange interaction is ferromagnetic for both the $B8_1$ and $B31$ structures, although it is much smaller in $B31$.[11,26] The BR model neglects the microscopic details of the exchange interaction and expresses the Curie temperature T_C only as a function of the volume V:

$$T_C = T_0\left[1 + \beta\frac{(V - V_0)}{V_0}\right], \tag{1}$$

where T_0 is the Curie temperature at the volume V_0, which is the volume in the hypothetical absence of exchange interaction (here the volume of the $B31$ structure above T_p). For certain values of the parameter β, Eq. (1) predicts a first-order phase transition between a ferromagnetic and paramagnetic state; however, the model does not explain the second-order phase transition at T_t and neither does a refinement of the theory introducing a term proportional to $(V-V_0)^2$.[27]

The first attempt at explaining the second-order phase transition is from Goodenough and co-workers, who postulated a high-spin to low-spin transition associated with the change of lattice structure from $B8_1$ to $B31$.[13,14] This, however, is not supported by neutron scattering, which measures little variation of the moment with the volume.[28] The MnAs

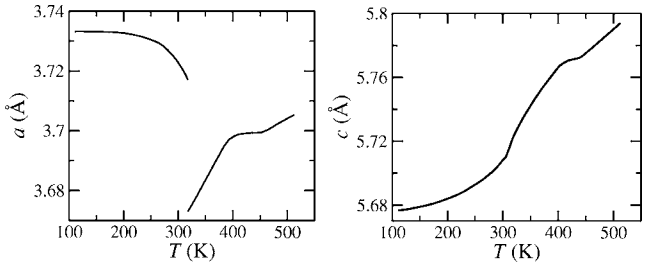

FIG. 5. Lattice parameters a and c (see Fig. 3) as a function of temperature (after Ref. 10).

unit cell volume in any phase is too big to justify a high-spin to low-spin transition. In $MnAs_{1-x}P_x$ the change from high spin to low spin is observed,[10,29,30] for volumes around 120 Å^3, while the unit cell of MnAs remains always larger than 130 Å^3. Another possible explanation of the second-order phase transition assumes a random distribution of distortions over the main $B8_1$ phase.[31] Again neutron diffraction invalidates this since regular $B8_1$ is found above T_t.[23]

Several phenomenological Landau-type models have been proposed.[24,32,33] In this case the correct thermodynamic behavior is obtained by construction but the theory contains a number of parameters to fit from experiments. The idea[24] is to expand the free energy Φ as a function of the the relative magnetization σ ($\sigma=1$ ferromagnetic state, $\sigma=0$ paramagnetic state) and the orthorhombic distortion d,[24]

$$\Phi(d,\sigma;T,H) = \Phi_0 + c_1[T - T_0(1 - \delta_1 d^2)]\sigma^2 + c_2\sigma^4 + c_3\sigma^6 + c_4(T - T_D)d^2 + c_5 d^4 - M_0\sigma H(1 - \delta_2 d^2), \tag{2}$$

where c_i and δ_i are coefficients, H is an external magnetic field, M_0 is the saturation magnetization, T_0 is the extrapolated Curie temperate of the low-temperature phase, and Φ_0 is a constant. Here the distortion d plays the same role as the relative change in volume $(V-V_0)/V_0$ of the BR model and the terms proportional to d^2 and d^4 drive the second-order phase transition. Variations over this scheme yield similar results.[32–34]

Spin fluctuation theory was also used for explaining the anomalous behavior of the susceptibility between T_p and T_t.[35,36] This qualitatively predicts an increase of the susceptibility when going from the $B31$ to the $B8_1$ structure, mainly associated with the fact that T_C increases with increasing temperature.

More recently tight-binding[37,38] and first-principles[39–47] calculations have been performed for MnAs in the $B8_1$ structure showing a general good agreement with experiments. We are aware of only two studies dealing with the $B31$ structure.[48,49] In Ref. 48 a description of the paramagnetic state of the $B31$ structure is given by assuming that it coincides with zero local magnetic moment of the Mn atoms. This in fact describes a low-spin state for Mn and not paramagnetism, which rather corresponds to constant magnetic moments randomly oriented by spin fluctuations.

The present work investigates the magnetic interactions across the various phase transitions of MnAs. An explanation of the magnetostructural properties in terms of first-principles calculations is given, thereby illustrating the origin and providing a justification of the parameters used by the different models.

III. RESULTS

A. DFT calculations

First-principles calculations within density functional theory are performed using the pseudopotential code based on localized atomic orbitals SIESTA.[50] The generalized gradient approximation (GGA) as parametrized in Ref. 51 is used for the exchange correlation potential, since it has been

TABLE I. Relaxed lattice parameters, local magnetic moment of the Mn and As atoms, and total energies per Mn atom for different spin configurations.

	a (Å)	b (Å)	c (Å)	V (Å^3)	u/b	v/c	$d_{2,1}$ (Å)	$d_{2,3}$ (Å)	μ_{Mn} (μ_{B})	μ_{As} (μ_{B})	$E-E_{\mathrm{FM}}$ (meV)
+ + + +	3.72	6.47	5.58	134.27	0.00	0.00	3.73	3.73	3.43	−0.24	0
+ + − −	3.56	6.18	5.81	127.93	0.00	0.00	3.56	3.57	3.10	0.00	62
+ − + −	3.55	6.24	5.62	124.54	0.05	0.05	3.10	4.10	3.01	−0.08	17
+ − − +	3.62	6.29	5.70	129.83	0.04	0.04	3.12	4.17	3.33	−0.03	35

shown to give good structural properties for hexagonal MnAs.[39,41,42] In the valence we consider 4s, 4p, and 3d orbitals for Mn and 4s, 4p, and 4d for As. For both Mn and As double-ζ-polarized local orbitals are used for the s and p angular momenta, whereas for the d orbitals double-ζ is used. The number of k points in the Brillouin zone is specified by a grid cutoff of 20 Å. This corresponds to a $11\times11\times8$ mesh for the $B8_1$ unit cell, giving approximately 1000 k points in the full Brillouin zone. For the $B31$ unit cell such a cutoff yields a $8\times11\times7$ mesh. The real-space mesh cutoff, which determines the density of the real-space grid, is 300 Ry.

After full relaxation of the unit cell to a pressure below 0.1 kbar and of the atomic positions to a force smaller than 0.01 eV/Å the $B31$ unit cell in the ferromagnetic configuration relaxes to a $B8_1$ structure with $a=3.72$ Å and $c=5.58$ Å. The experimental values at room temperature are $a=3.724$ Å and $c=5.707$ Å. Therefore the relative error is below 1% for a and −2% for c. The lattice parameters at 110 K can be extracted from Fig. 5 and are $a=3.733$ Å and $c=5.677$ Å. This demonstrates that GGA-DFT reproduces rather well the zero-temperature ground state.

For a fixed c/a ratio of 1.54, which is close to the experimental value at the first-order phase transition, the energy is minimized for $a=3.695$ Å, which compares well with the results of other *ab initio* calculations.[39,41,42] Also the band structure and the density of states are similar to previous calculations. The magnetic moment per Mn atom is $3.4\mu_{\mathrm{B}}$ and compares well with the measured value of $3.4\mu_{\mathrm{B}}$.

The unit cell of the $B31$ structure contains four Mn atoms, allowing for three possible independent antiferromagnetic configurations of the local moments of the Mn atoms. The different antiferromagnetic states are $++--$, $+-+-$, and $+--+$. As a matter of notation $++--$ means that atoms 1 and 2 in the unit cell have opposite magnetic moment than that of atoms 3 and 4. The indices of the Mn atoms in the unit cell are defined in Fig. 3(b). A cell relaxation is performed for those three antiferromagnetic configurations. Table I lists the obtained relaxed structures together with the total energies per Mn atom as compared to the ferromagnetic ground-state energy ($E-E_{\mathrm{FM}}$). The structure remains of the $B8_1$ type if the local moments are ferromagnetically aligned in the hexagonal plane, whereas it changes to the $B31$ type if the moments are antiferromagnetically aligned, with $u(v)$ of the order of $0.05b(c)$. There is also a slight displacement of the Mn atoms along **c** of at most $0.01c$ and of the As atoms along **b** of at most $0.01b$. Generally it can be observed that the in-plane lattice parameters contract and the c parameter expands for the antiferromagnetic states, resulting in a net reduction of the volume V.

The calculated lattice parameters are similar to those given in Ref. 48, although the absolute value of the magnetic moments differs. This is probably due to the fact that we use a Mulliken population analysis to determine the local magnetic moment, while in the reference it is obtained by integrating the magnetization density over a sphere around the Mn atoms.

The total energy for the ferromagnetic alignment is the lowest, although the $+--+$ configuration is higher of only 17 meV/Mn. This indicates that the system should evolve to one of the antiferromagnetic states under pressure, since those have a much smaller volume but only a slightly higher energy.

Table I gives also the distances between a Mn atom and its first three nearest-neighbor Mn atoms in the hexagonal plane $d_{2,1}$, $d_{2,2}$, and $d_{2,3}$ (see Fig. 4). Note that $d_{2,2}=a$ and it is not given explicitly. While these distances are all equal in the hexagonal case, they differ by as much as 1 Å in the $B31$ structure. Large changes in the distance between the Mn atoms are possible since the nearest-neighbor Mn-Mn separation in MnAs is well above the interatomic distance 2.61 Å of bulk Mn,[52] which can be regarded as the minimal possible distance between Mn atoms. The distance between nearest-neighbor Mn and As atoms lies between 2.46 Å and 2.62 Å for all the different configurations and changes therefore much less than the Mn-Mn distance.

The local magnetic moment on the Mn (μ_{Mn}) and As (μ_{As}) atoms, calculated using the atomic Mulliken population,[53] is also given in Table I. The local moment on the Mn atoms ranges between $3.43\mu_{\mathrm{B}}$ for the ferromagnetic configuration to $3.01\mu_{\mathrm{B}}$ for the $+-+-$ configuration. This reduction in the local moment is mainly due to the decrease of the cell volume and the consequent increase of the hybridization between the Mn-d and As-p orbitals.

In summary these calculations show that the distortion to the $B31$ structure is caused by an antiferromagnetic alignment of the local magnetic moments in the hexagonal plane.

B. Fit to the Heisenberg energy

In order to extract the various exchange parameters, calculations are performed for three different $B31$ supercells in different local magnetic configurations. These supercells contain eight Mn atoms and are obtained by doubling the $B31$ unit cell along the **a** lattice vector (supercell 1), along **b** (supercell 2), and along **c** (supercell 3). The calculated total energies are then fitted to a model Heisenberg energy

$$E_{\mathbf{s}_1,\mathbf{s}_2,\ldots} = E_0 - \frac{1}{2}\sum_{i,j} \mathbf{s}_i \mathbf{s}_j J_{ij}, \tag{3}$$

where $\mathbf{s}_i$ is the magnetic moment normalized to $1(|\mathbf{s}_i|=1)$ and the J's are coupling parameters. Here we neglect four-moment coupling constants J_{ijkl} and the small induced magnetic moment over the As atoms. E_0 is a constant that can be associated with the energy of a paramagnetic phase. In fact, if all the local magnetic moments are randomly aligned, the contribution coming from $\Sigma_{i,j}\mathbf{s}_i\mathbf{s}_j J_{ij}$ vanishes.

In mean-field theory the Curie temperature T_C for classical Heisenberg exchanged magnetic moments is

$$k_B T_C = \sum_j J_{0j}/3 = J_0/3, \tag{4}$$

where k_B is the Boltzmann constant. The quantity $J_0=\Sigma_j J_{0,j}$ is the sum of the exchange coupling constants of a given magnetic moment with all the other moments. In the following sections Eq. (4) is always used to extract Curie temperatures, although it is well known that the mean-field approximation overestimates T_C.[54]

Calculations are performed for all the independent spin configurations of the supercell 1 and for a randomly chosen subset of those of supercells 2 and 3. Thirty-five different configurations of the magnetic moments are used in total. The energies are then fitted by a least-mean-squares fit to the coupling parameters of Eq. (3). Since the system is metallic with the d orbitals having finite density of states at the Fermi level, the magnetic interaction is expected to have a long-range character. For the chosen supercells it is possible to extract coupling constants up to the ninth nearest neighbor. The lattice parameters used are approximately those for ferromagnetic MnAs in the $B8_1$ structure at the phase transition temperature T_p=318 K (a=3.71 Å, c/a=1.54).

We carefully tested the convergence of our results with the range of the Heisenberg exchange interaction. Figure 6 shows the standard deviation Δ of the energies resulting from Eq. (3) as compared to the calculated DFT energies per Mn atom, the value of E_0 per Mn atom, the mean-field Curie temperature T_C, and J_0 as a function of the number of coupling coefficients, N_{max}, included in the fit. The standard deviation Δ decays monotonically, remains roughly constant for $N_{max}\geqslant 3$, and then reaches a minimum value of around 5 meV for N_{max}=9. This can be considered as the error resulting from neglecting high-moment coupling constants. The value of E_0 changes less over the whole range, being something like an average of the energies of the different magnetic configurations. T_C reaches a constant value of approximately 633 K for $N_{max}\geqslant 3$. This indicates that the main contribution arises from the first three nearest-neighbor coupling constants. The experimental value of T_C for the low-temperature phase lies between T_p=318 K and T_t=400 K. This means that our mean-field T_C overestimates the experimental one by a factor between 1.6 and 2.

Figure 7 shows the calculated exchange coupling constants as a function of the distance for two different fits counting, respectively, third- and ninth-nearest-neighbor coupling. The first three exchange constants J_1, J_2, and J_3 [see Fig. 8(a)] remain nearly unchanged when going from third-

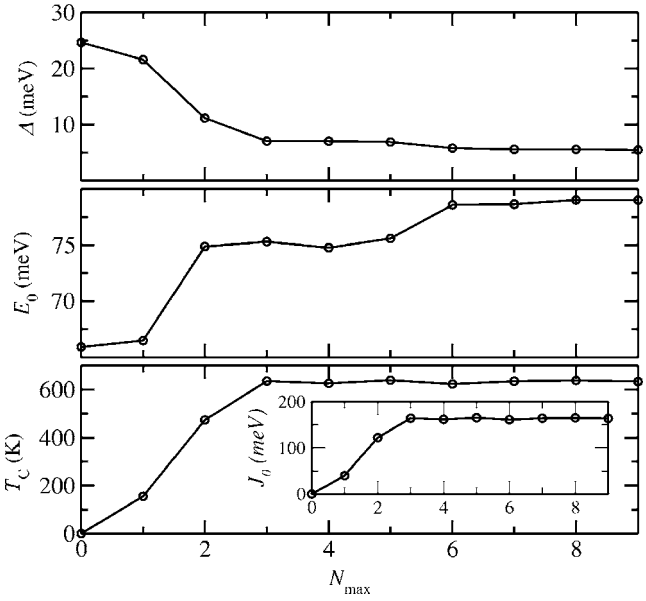

FIG. 6. Variation of the various exchange quantities as function of the number of coupling coefficients, N_{max}, included in the fit. (a) Standard deviation Δ of the energies resulting from Eq. (3) as compared to the calculated DFT energies per Mn atom. (b) E_0 per Mn atom [Eq. (3)], where the zero of energy is chosen as the energy of the ferromagnetic state. (c) Mean-field Curie temperature T_C.

to ninth-nearest-neighbor coupling. Interestingly the coupling parameters are positive and therefore ferromagnetic up to $d\sim 6.5$ Å (fifth-neighbor interaction). In what follows we consider only coupling parameters up to third nearest neighbors, as they give the main contribution to the properties of the material.

C. $B8_1$ to $B31$ distortion at T_p

The $B8_1$ to $B31$ structure phase transition at T_p is investigated by calculating the Heisenberg coupling constants for different distorted cells. We start from $B8_1$ with the experimental lattice parameters near T_p (a=3.71 Å, $b=\sqrt{3}a$, c =1.54a, $u=v=0$) and distort the cell linearly to the $B31$ structure. The amount of distortion d is given in percent,

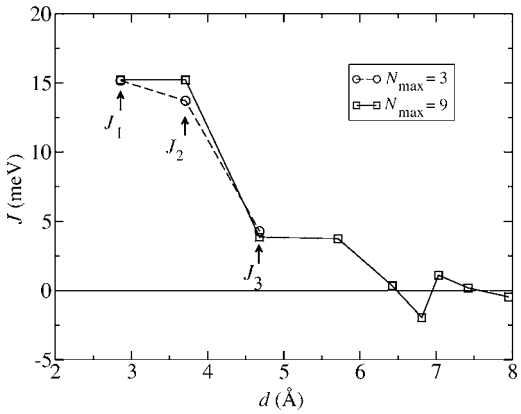

FIG. 7. Exchange coupling parameters for N_{max}=3 and N_{max} =9 as a function of the distance between the magnetic moments.

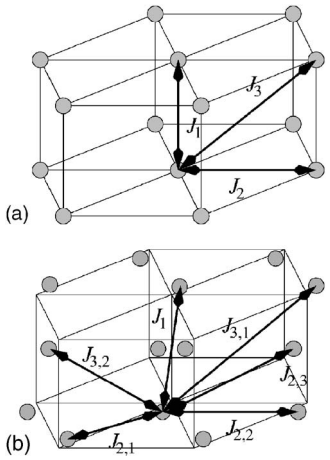

FIG. 8. Schematic representation of the atomic positions of the Mn atoms together with the exchange constants for the $B8_1$ (a) and $B31$ (b) structures.

where $d=0\%$ stands for the lattice parameters of the ferromagnetic $B8_1$ cell just below T_p and $d=100\%$ for the paramagnetic $B31$ cell above T_p ($a=3.676$ Å, $b=1.01\sqrt{3}a$, $c=1.556a$, $u=2.71\times10^{-2}b$, $v=2.45\times10^{-2}c$).[23] Calculations are done for distortions between 0% and 220%. Note that the volume decreases with increasing distortion. For these calculations only supercells 1 and 2 are used with a total of 26 different spin configurations. The standard deviation of the fit is approximately constant for all the distortions and is of the order of 5 meV/Mn.

Figure 8(a) shows the Mn atoms of the $B8_1$ structure coupled by first- (J_1), second- (J_2), and third- (J_3) nearest-neighbor interactions. In the distorted $B31$ structure the three coupling constants J_1, J_2, and J_3 are split into six different constants due to symmetry loss. While there is still only one J_1 coupling, the in-plane J_2 splits into three different coupling constants $J_{2,1}$, $J_{2,2}$, and $J_{2,3}$, corresponding to different distances between the Mn atoms in the hexagonal plane (see Fig. 4). Moreover, also the third-nearest-neighbor coupling J_3 splits into three different constants, although two of them are between Mn atoms separated by approximately the same distance at T_p, and so they are assumed to be identical. Hence J_3 effectively splits only into $J_{3,1}$ and $J_{3,2}$.

Figure 9 shows the calculated values for the exchange parameters as a function of the distortion. For 0% distortion the values of $J_{2,1}$, $J_{2,2}$, and $J_{2,3}$ are approximately equal, reflecting the hexagonal symmetry. The values of $J_{3,1}$ and $J_{3,2}$ also should be identical although they differ by about 2 meV (note that in the fit we do not force the $B8_1$ symmetry, when determining the J's for the undistorted structure). This can be assumed to be the error over the fit. Additional control fits were also performed for different subsets of the 26 spin configurations. The variation over the J was of 20%, whereas the variation of J_0 was always smaller than 6%.

The value of J_1 remains approximately constant for all the distortions, reflecting the fact that the distance between the quasihexagonal layers remains roughly constant. In contrast the in-plane J's change and eventually become antiferromagnetic. In particular the coupling becomes strongly antiferromagnetic for $J_{2,1}$—i.e., for those Mn atoms that get closer in

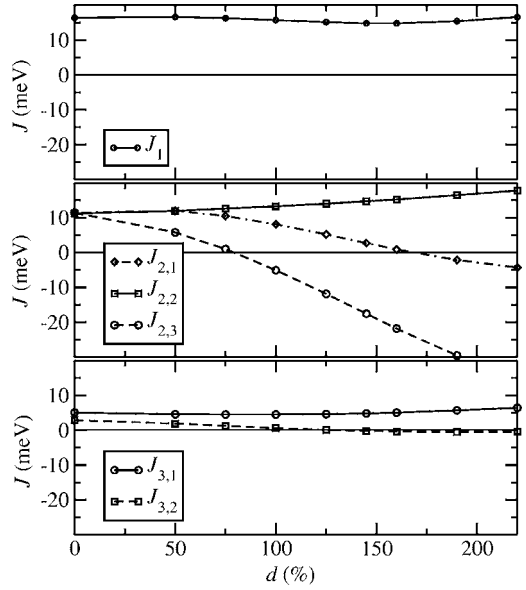

FIG. 9. Evolution of the exchange coupling constants when distorting the unit cell linearly from the $B8_1$ structure to the $B31$ structure. $d=0\%$ represents the $B8_1$ structure at $T_p=318$ K, $d=100\%$ represents the $B31$ structure at T_p. A positive (negative) value of J means ferromagnetic (antiferromagnetic) coupling.

the hexagonal plane under distortion. Also $J_{2,3}$, which couples the Mn atoms increasing their separation, is reduced and becomes antiferromagnetic for large distortions. Finally the coupling parameters $J_{3,1}$ and $J_{3,2}$ have only minor changes, with $J_{3,1}$ becoming weakly antiferromagnetic for large distortions.

The evolution of the coupling constants with the distortion indicates why for the $+-+-$ and $+--+$ spin configurations (see Table I), where the spins are antiferromagnetically aligned in the hexagonal planes, the lowest energy is found for the $B31$ structure. The relaxed structure for both spin configurations is similar to a distortion of about 200%. At this distortion the in-plane coupling constants $J_{2,1}$ and $J_{2,3}$ become antiferromagnetic, resulting in a reduction of the total energy as compared to the $B8_1$ structure for those spin configurations. In contrast for the $++++$ and $++--$ configurations, which have a ferromagnetic alignment of the moments in the hexagonal plane, the $B8_1$ structure is stable, since for that structure $J_{2,1}$ and $J_{2,3}$ are positive.

Figure 10 shows the relative change of the mean-field Curie temperature $T_C(d)/T_C(0)$ for the ferromagnetic state. T_C decreases monotonically with increasing distortion. For 100% distortion ($B31$ structure at T_p) $T_C(100\%)/T_C(0)=0.67$, demonstrating that when the phase transition from the $B8_1$ to the $B31$ structure occurs, the system in the $B31$ cell is already paramagnetic with very little magnetic order. The experimental Curie temperature T_C^{expt} for the hexagonal cell at $T=T_p$ is not known, since the structure changes.

Figure 10 also shows the total energy per $B31$ unit cell as a function of the distortion in the ferromagnetic (FM) and in the $+--+$ antiferromagnetic (AF) configurations. This latter is the antiferromagnetic configuration giving the lowest total energy at its minimum among all the ones calculated along the considered distortion. The figure also shows the

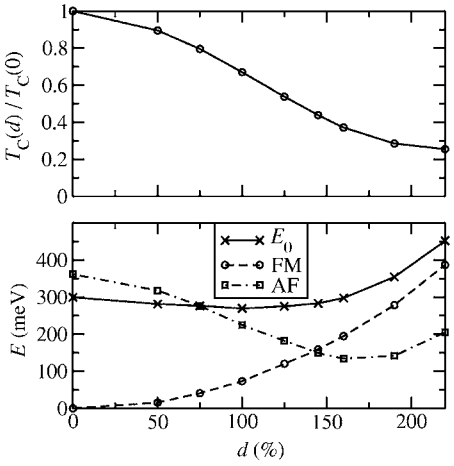

FIG. 10. Top figure: relative change of the mean-field Curie temperature $[T_C(d)-T_C(0)]/T_C(0)$ for the ferromagnetic state. Bottom figure: total energy for one $B31$ unit cell for the ferromagnetic configuration (FM), for the $+--+$ antiferromagnetic configuration (AF), together with E_0 [Eq. (3)], as a function of the distortion d. $d=0\%$ and $d=100\%$ represent, respectively, the $B8_1$ and $B31$ phases at $T_p \approx 318$ K.

value of E_0, the energy of the paramagnetic state [see Eq. (3)]. The zero in the energy scale is the energy of the ferromagnetic state for $d=0\%$.

The ferromagnetic state has its energy minimum for $d=0\%$ and increases parabolically for increasing distortion. This means that the $B8_1$ structure is the one with lowest energy in the ferromagnetic state. In contrast the competing antiferromagnetic configuration has a minimum for about 180% distortion, where the energy is lower than the ferromagnetic phase. The crossing between the two energy curves occurs at about $d \approx 142\%$. The ground state of the system is therefore expected to be ferromagnetic below this distortion and to become antiferromagnetic above this distortion.

E_0 has a very flat minimum for distorted cells, reflecting the fact that the total energy increases for the ferromagnetic state, but decreases on average for the antiferromagnetic states. The minimum is found to be at about $d \approx 100\%$, which corresponds indeed to the lattice parameters of the paramagnetic state above the phase transition. This is suggestive of a structural change from the $B8_1$ to $B31$ structure in correspondence with the onset with the paramagnetic state.

D. $B31$ to $B8_1$ distortion at T_t

For temperature in between T_p and T_t the MnAs crystal structure continuously changes from $B31$ to $B8_1$. As mentioned in Sec. II the phase transition temperature T_t is usually identified as the temperature where the susceptibility and specific heat have a maximum. This is at about 398 K. However, the distortion should disappear at slightly higher temperatures as pointed out in Ref. 24. Therefore, since the exact temperature for this second-order structural phase transition is not known exactly, we introduce an operative definition and assume that the distortion disappears at a temperature T_s, at which the slope of the in-plane lattice constant as a function of temperature $a(T)$ changes discontinuously (see Fig. 5). According to Fig. 5 the lattice constant at T_s is $a(T_s)=\tilde{a} \approx 3.699$ Å and $(\partial a/\partial T)_{T_s} \approx 0$. At T_t the same lattice parameter is $a(T_t) \approx 3.697$ Å, so that the difference in $\tilde{a}$ is very small.

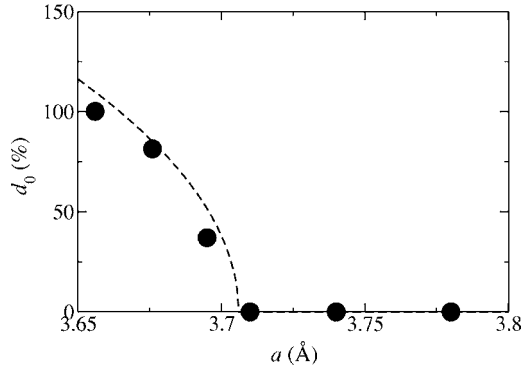

FIG. 11. Distortion d_0 for the minimum of the paramagnetic ground state as a function of the lattice constant a. The dots are calculated values; the dashed line is a fit with Eq. (5).

The main reason for the second-order phase transition at high temperatures is related to the lattice thermal expansion. The idea is that upon volume expansion, the ground state of the paramagnetic phase moves towards the hexagonal structure. We verify this hypothesis by calculating the minimum of E_0 ($E_0^{\min}$) along a distortion of the cell transforming $B8_1$ to $B31$. In the calculation the volume of the cell is kept constant and we repeat the calculation for different volumes. This allows us to evaluate both $E_0^{\min}$ and the corresponding distortion as a function of the volume. Since for $T>T_p$ MnAs is always paramagnetic, then the minimum of E_0 corresponds to the stable distortion d_0 at a given volume. In practice the change in volume can be described simply by the change in the planar lattice constant a, since both b/a and c/a do not deviate much from their value at T_p. Thus we always consider $b=\sqrt{3}a$ and $c=1.556a$ and the phase transition is investigated as a function of a only.

The equilibrium distortion d_0 as a function of a is presented in Fig. 11. Indeed the distortion decreases with volume and it disappears for a between $a=3.695$ Å and $a=3.71$ Å. Moreover, we find 100% distortion for $a \sim 3.66$ Å. These values agree rather well with the experimental ones, where the distortion disappears at about $a(T_s)=3.699$ Å and 100% distortion is found at $a(T_p)=3.673$ Å.

In order to interpret these results consider that the distortion is symmetric for $\pm d$ $[E_0(d)=E_0(-d)]$, and therefore E_0 can be expanded in even powers of the distortion, $E_0(d)=r_0+r_1\,d^2+r_2\,d^4$. Here r_i are parameters to fit to the DFT calculations. In particular note that r_0 corresponds to the energy of the paramagnetic phase when the crystal is undistorted; i.e., it has hexagonal structure. In this way the minimum of the $E_0(d)$ curve is obtained for $d_0=\sqrt{-\frac{r_1}{2r_2}}$ if $r_1<0$, and for $d_0=0$ for $r_1 \geqslant 0$. We now define $\tilde{a}$ as the lattice constant where $r_1=0$. For small distortions the parameters r_1 and r_2 can then be further expanded around $\tilde{a}$ as $r_1=r_{1,1}(a-\tilde{a})$ and $r_2=r_{2,0}+r_{2,1}(a-\tilde{a})+r_{2,2}(a-\tilde{a})^2$. In order to obtain the leading terms in this expansion, we calculate the values of r_0,

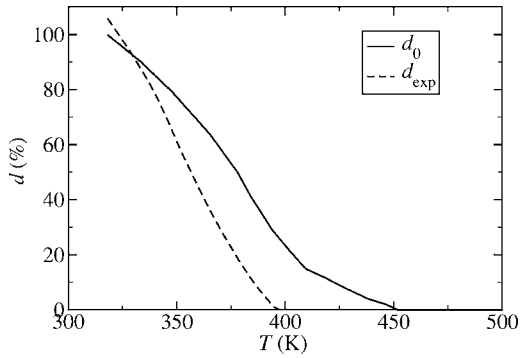

FIG. 12. Solid line: distortion d_0 for the minimum of the paramagnetic ground state as a function of temperature calculated with Eq. (5) (with γ=1184 and $\tilde{a}$=3.699 Å) using $a(T)$ taken from Fig. 5. Dashed line: experimental distortion extracted from $v(T)$ of Fig. 3 in Ref. 10.

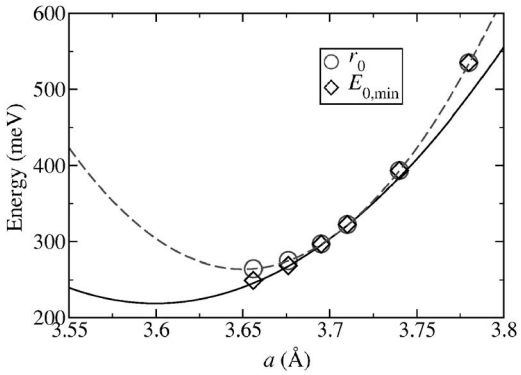

FIG. 13. Energy expansion coefficient r_0 and $E_{0,\min}$ as a function of the lattice constant. The dashed line shows $\epsilon_0+\epsilon_1\ (a-a_0)^2$; the solid line shows $\epsilon_0+\epsilon_1\ (a-a_0)^2-\epsilon_2\ (a-\tilde{a})^2$ [see Eq. (6)].

r_1 and r_2 for different lattice constants (a=3.656, 3.676, 3.695, 3.71, 3.74 and 3.78 Å). We then first calculate $\tilde{a}$ and $r_{1,1}$ by mapping r_1 onto the expansion $r_1(a)=r_{1,1}(a-\tilde{a})$, and with the obtained value of $\tilde{a}$ we can then in the same way also calculate the expansion coefficients of r_2. The so calculated values for the leading terms are $\tilde{a}$=3.706 Å, $r_{1,1}$ =62.4×10^{-3} meV/Å, and $r_{2,0}$=1.29×10^{-7} meV (d is given in percent). The equilibrium distortion d_0 up to first order in a is then

$$d_0(a) = \gamma\sqrt{\frac{\tilde{a}-a}{\tilde{a}}}\Theta(\tilde{a}-a), \quad \gamma = \sqrt{\tilde{a}\frac{r_{1,1}}{2r_{2,0}}}, \tag{5}$$

where $\Theta(x)$ is the Heaviside function. With the values of $\tilde{a}$, $r_{1,1}$, and $r_{2,0}$ given above γ=947 is obtained. The resulting distortion is presented in Fig. 11.

Interestingly, if we use Eq. (5) to fit the experimentally determined distortions at $a(T_s)$=3.699 Å (d_0=100%) and $a(T_p)$=3.673 Å (d_0=0), we obtain γ=1184 and $\tilde{a}$=3.699, both in good agreement with our calculated values. This suggests that the main effects of the distortion to the $B31$ structure arise from the atomic displacement from the symmetry positions and that small changes of the ratio of the lattice vectors, neglected in our calculations, play only a secondary role. Using the values γ=1184 and $\tilde{a}$=3.699 Å of the two parameters the evolution of the distortion as a function of temperature T can be obtained by inserting the data for $a(T)$ from Fig. 5 in Eq. (5). The result is shown in Fig. 12. It also shows the experimental distortion d_{expt} obtained from $v(T)$ extracted from Fig. 3 of Ref. 10. The main difference between the two curves is that the distortion d_{expt} becomes zero at 398 K, whereas in our results this happens only at 450 K. This is due to our choice of T_s=450 K, which by definition sets the temperature where the distortion disappears. Close to the phase transition temperature fluctuations play an important role, so that for very small distortions close to the phase transition the description may not be valid.

By using the computed values of r_0, r_1, and r_2 the minimum of E_0 [$E_0^{\min}=E_0(d=d_0)$] is calculated as a function of the volume of the unit cell, and it is shown in Fig. 13 together with r_0. Recalling that r_0 is the energy of the paramagnetic hexagonal phase, it also can be expanded as a function of the lattice constant $r_0=\epsilon_0+\epsilon_1\ (a-a_0)^2$, where a_0 is the equilibrium lattice constant of the hexagonal phase. This, combined with Eq. (5), gives an expression for the energy minimum as a function of the lattice constant a:

$$E_0^{\min}(a) = \epsilon_0 + \epsilon_1(a-a_0)^2 - \epsilon_2(a-\tilde{a})^2\Theta(\tilde{a}-a),$$

$$\epsilon_2 = \frac{r_{1,1}^2}{4r_{2,0}} = 7546\frac{\text{meV}}{\text{Å}^2}, \tag{6}$$

where ϵ_0, ϵ_1, and a_0 are to be fitted from the calculations of r_0 (Fig. 13). The fitted values are ϵ_0=264 meV, ϵ_1 =15 935 meV/Å^2, and a_0=3.65 Å. From Eq. (6) the energy minimum is easily found,

$$a_{\min} = a_0\left(1 - \frac{\epsilon_2}{\epsilon_1-\epsilon_2}\frac{\tilde{a}-a_0}{a_0}\right), \tag{7}$$

and by using the calculated parameters we estimate $a_{\min}$ =3.60 Å. Since $a_{\min}<a_0$, we derive the important result that the distortion allows the volume to be further reduced as compared to the hexagonal phase. Furthermore, the curvature of the energy as a function of a is

$$\frac{\partial^2 E_0^{\min}(a)}{\partial a^2} = 2\epsilon_1 - 2\epsilon_2\Theta(\tilde{a}-a), \tag{8}$$

which is also reduced by a factor of $2\epsilon_2$ when the structure is distorted.

The effect of the thermal expansion on the lattice parameter can now be modeled as a temperature-dependent position of a_0, $a_0=a_0(T)$. The change of the lattice constant with temperature for the distorted phase can therefore be written as

$$\frac{\partial a_{\min}}{\partial T} = \frac{\epsilon_1}{\epsilon_1-\epsilon_2}\frac{\partial a_0}{\partial T}. \tag{9}$$

Since ϵ_2 is smaller than ϵ_1, the lattice expands with temperature faster for the distorted phase than for the undistorted phase. If the calculated values for ϵ_1 and ϵ_2 are used, the

ratio $\epsilon_1/(\epsilon_1-\epsilon_2)$ is found to be 1.90, which agrees well with the value of 2.25 extracted from Fig. 5. Near the phase transition—i.e., where $d\approx 0$—phononic effects due to the different curvatures of the energy and fluctuations should be considered. It is especially interesting that the change of the lattice constant with temperature goes to zero near the phase transition temperature.

In the same way as E_0 also T_C can be expanded as a function of the lattice constant and of the distortion:

$$T_C(a,d) = T_C(\tilde{a})\left[1 + K_v\frac{a-\tilde{a}}{\tilde{a}} - K_d d^2\right], \tag{10}$$

where K_v and K_d are parameters and $T_C(\tilde{a})$ is the Curie temperature for the cell with lattice parameter $\tilde{a}$ and where the atoms are in the hexagonal positions. The parameters are fitted by a least-mean-squares fit to the calculated values of T_C obtained for six lattice constants ranging between 3.656 Å and 3.78 Å and for different distortions. We obtain $T_C(\tilde{a})=573$ K, $K_v=6.80$, and $K_d=2.62\times 10^{-5}$. At $d=100\%$ the relative change of the Curie temperature is $T_C(\tilde{a},d=100\%)/T_C(\tilde{a})=0.74$ and corresponds roughly to the value of Fig. 10. In this case it is slightly larger due to the fact that the volume is kept constant, whereas for the calculations of Fig. 10 it shrinks with increasing the distortion.

Next we calculate the dependence of the magnetic moment on the distortion and on the unit cell volume. The dependence is again expanded to lowest order in a and d:

$$\mu(a) = \mu(\tilde{a})\left[1 + \alpha_\mu\frac{a-\tilde{a}}{\tilde{a}} + \alpha_{\mu,d}d^2\right]. \tag{11}$$

We now have different ways of extracting the magnetic moment of the Mn atoms from our DFT calculations. One possibility is to take the total moment of the cell for the ferromagnetic spin configuration and divide it by the number of Mn atoms. In this way, however, the small induced moments of the As atoms are subtracted from the moment on the Mn. A second possibility is to take the average Mulliken spin population for the Mn atoms. The advantage of this method is that also antiferromagnetic configurations can be used to determine the average moment and the induced moments of the As atoms are accounted for. The drawback, however, is that Mulliken populations are somewhat arbitrary as they depend on the basis set.

By setting $\tilde{a}$ to 3.699 Å, the values obtained using the cell moment are $\mu(\tilde{a})=3.28\mu_B$, $\alpha_\mu=3.28$, and $\alpha_{\mu,d}=-1.15\times 10^{-6}$. Similarly from the average Mulliken population over all the magnetic configurations we obtain $\mu(\tilde{a})=3.42\mu_B$, $\alpha_\mu=3.48$, and $\alpha_{\mu,d}\approx 0$. These results are rather similar to each other. With $\alpha_\mu=3.28$ and $\alpha_{\mu,d}=-1.15\times 10^{-6}$ a reduction of the lattice constant of 1%, as approximately found at T_p, results in a reduction of the magnetic moment of about 3% and a distortion of $d=100\%$ results in a reduction of μ of about 1%. Both effects therefore reduce the magnetic moment and are of the same order of magnitude.

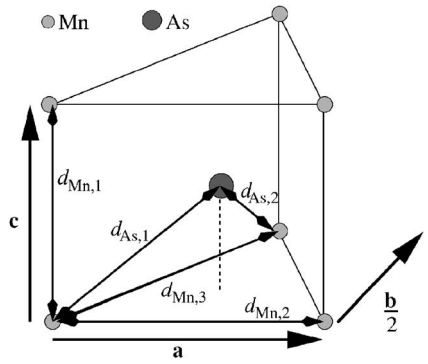

FIG. 14. Diagram of the positions of Mn and As atoms in orthorhombic MnAs.

E. Small distortions of the $B8_1$ structure

In this section the dependence of T_C on the individual lattice parameters and on the distances between the atoms is investigated for the $B8_1$ structure. Our approach is to distort the cell orthorhombically but to leave the atoms in their high-symmetry positions. Apart from a general understanding of the phase diagram of MnAs this analysis is useful for predicting the behavior of MnAs when grown on a substrate. For instance when grown on GaAs(001) the substrate induces strain in MnAs, and the unit cell is slightly orthorhombically distorted.[1] This distortion does not correspond to the orthorhombic $B31$ structure, since the atoms do not move out of the high-symmetry positions. Moreover, different growth orientations are possible and the Curie temperature varies accordingly.[7] In addition Ref. 8 presents experimental results showing that the phase transition temperature T_p changes when strain is applied to the MnAs film. In that article we have compared our theoretical predictions for the dependence of T_p on the lattice distortion with the experimental findings. In this section we refine and expand our previous analysis.

When the cell is orthorhombically distorted the first three nearest-neighbor coupling constants split into five different constants, corresponding to the ones of the $B31$ cell (Fig. 8) and with the only exception that now $J_{2,1}=J_{2,3}$. The number of total energy calculations for the fit of the coupling parameters is 16. The change of T_C for each different distortion can be expressed as a function of the change of each single Mn-Mn and Mn-As distance in the unit cell. This gives

$$\frac{\delta T_C}{T_C} = \frac{\delta J_0}{J_0} = \sum_{\mu=1}^{5} K_\mu N_\mu \frac{\delta d_\mu}{d_\mu}, \tag{12}$$

where the sum goes over all five independent distances in the orthorhombic unit cell as defined in Fig. 14. The dependence on the angles between the atoms is neglected. N_μ are the multiplicities of each distance d_μ within one unit cell and have the values $N_{Mn,1}=4$, $N_{Mn,2}=4$, $N_{Mn,3}=8$, $N_{As,1}=4$, and $N_{As,2}=8$. For the evaluation of the coefficients K_μ, 21 different distortions are considered, including changes of volume, changes of the ratio of the different axes, and different displacements of the As atoms. For all the distortions the ortho-

rhombic symmetry, however, was preserved. The best fit for K_μ gives

$$K_{\mathrm{Mn},1}=6.6, \quad K_{\mathrm{Mn},2}=6.2, \quad K_{\mathrm{Mn},3}=5.9,$$

$$K_{\mathrm{As},1}=-7.5, \quad K_{\mathrm{As},2}=-7.5. \tag{13}$$

The values of $K_{\mathrm{Mn},1}$ and $K_{\mathrm{Mn},2}$ are almost identical, as one should expect from the symmetry and similarly for $K_{\mathrm{As},1}$ and $K_{\mathrm{As},2}$.

Equation (12) describes the fact that the change of T_C is the result of an interplay between the change of the Mn-Mn and Mn-As distances. The calculated K_μ show that, while an increase in the distance between Mn atoms increases T_C, an increase of the Mn-As distance decreases it. However, note that the two distances cannot be changed independently; thus, the net change in T_C depends on the details of the distortion.

J_0 can also be expanded over the orthorhombic lattice parameters

$$\frac{\delta J_0}{J_0}=\sum_{i=1}^{3} K_i \frac{\delta a_i}{a_i}, \tag{14}$$

with

$$K_i=\sum_{\mu=1}^{5} K_\mu N_\mu \frac{a_i}{d_\mu}\frac{\partial d_\mu}{\partial a_i},$$

where $a_1=a$, $a_2=b$, and $a_3=c$. The change of the distances between Mn and As atoms is not exactly known for the orthorhombic cell. However, it is easy to show that in first approximation the position of the As atom in the cell does not influence J_0, since up to first order $\delta d_{\mathrm{As},2}=2\delta d_{\mathrm{As},1}$ when moving the As atom inside the cell. Therefore the As atoms can be assumed to remain in the high-symmetry position. Assuming now $K_{\mathrm{Mn},2}=K_{\mathrm{Mn},3}$ and $K_{\mathrm{As},1}=K_{\mathrm{As},2}$ (as imposed by symmetry), the general form of the K_i is

$$K_a=K_b=6K_{\mathrm{Mn},2}+\frac{96K_{\mathrm{As},1}}{16+3\tilde{c}^2},$$

$$K_c=4K_{\mathrm{Mn},1}+\frac{36K_{\mathrm{As},1}\tilde{c}^2}{16+3\tilde{c}^2}, \tag{15}$$

where $\tilde{c}=c/a$. Using the average between $K_{\mathrm{Mn},2}$ and $K_{\mathrm{Mn},3}$ and $\tilde{c}=1.533$ this gives

$$K_a=K_b=4.9, \quad K_c=-1.0. \tag{16}$$

Our results clearly show that stretching the unit cell along the basal plane raises T_p (since $K_a>0$), while stretching along the c axis lowers T_p ($K_c<0$). An increase of the volume without distorting the cell results in an increase of the ferromagnetic exchange interactions and therefore of T_C, since K_a is positive and larger in magnitude than K_c. The results for K_a and K_b differ slightly from the ones given in Ref. 8, since in that case we did not constrain K_a to be equal to K_b. If the cell changes only its volume, the expansion corresponds to the one of Eq. (10) with a factor $K_v=2K_a+K_c=8.8$. We note that this value is somewhat different from the value of $K_v=6.8$ given in Sec. III D. This is due to the different type of analysis performed in this section, which starts from the dependence of T_C on the distances between the single atoms. The difference is, however, small and can be considered a measure for the error in our results.

IV. DISCUSSION

It is now possible to analyze two peculiar properties of MnAs. The first is the anomalous behavior of the susceptibility χ as a function of temperature between T_p and T_t. The second is the fact that although the Curie temperature for ferromagnetic MnAs has to be larger than T_p, the T_C extrapolated from the susceptibility above T_t is only 285 K.[13] In this section both these features are explained using the dependence of the susceptibility on the Curie temperature [$\chi=\chi(T_C)$] and the strong dependence of the Curie temperature on the lattice parameters found in the previous sections [$T_C=T_C(a,b,c,d)$]. $T_C(T)$ and $\chi(T)$ are therefore determined using the experimentally measured temperature dependence of the lattice vectors $a(T)$, $b(T)$, and $c(T)$ and of the distortion $d(T)$. This analysis also provides a tool for extracting the parameters K_v and K_d from experimental data.

By generalizing Eqs. (10) and (14) the Curie temperature $T_C(a,b,c,d)$ can be written as

$$T_C(a,b,c,d)=T_{C,0}\left[1+K_a\left(\frac{a-\tilde{a}}{\tilde{a}}+\frac{b-\tilde{b}}{\tilde{b}}\right)+K_c\frac{c-\tilde{c}}{\tilde{c}}-K_d d^2\right], \tag{17}$$

where we use the fact that $K_a=K_b$ and we take the values for K_a and K_c from Eq. (16), while $K_d=2.62\times10^{-5}$ and $T_{C,0}=T_C(\tilde{a})=573$ K are calculated in Sec. III D. The reference lattice parameters are chosen to be the lattice vectors at T_s ($\tilde{a}=3.699$ Å, $\tilde{b}=\sqrt{3}\tilde{a}$, $\tilde{c}=1.56\tilde{a}$).

Similarly to the Curie temperature also the susceptibility is calculated in the mean-field approximation. This is justified for $T\gg T_C$, a condition which is satisfied for paramagnetic MnAs. The molar susceptibility χ_M is then given by

$$\chi_M^{-1}=\frac{1}{C_0}(T-T_C),$$

$$C_0=\frac{N_A\mu_B^2 g^2}{3k_B}s(s+1). \tag{18}$$

N_A is the Avogadro's number, $g\approx2$ is Lande's factor for the free electron spin, k_B is the Boltzmann constant, and s is the atomic total spin. Note that the susceptibility has an additional temperature dependence since T_C and s depend on the temperature through the lattice distortion. However, in what follows we neglect the dependence of s on the lattice parameters so that C_0 is constant over all temperature. An analysis performed by relaxing this approximation gives similar results.

Similarly to Sec. III D the model is further simplified by assuming that b/a and c/a are constant above T_p. As indicated in Eq. (5), d is a function of the lattice constant, $d(a) = \gamma\sqrt{(\tilde{a}-a)/\tilde{a}}\Theta(\tilde{a}-a)$. Moreover, we have shown that the experimental distortion as a function of the lattice constant is well reproduced when $\gamma=1184$. Therefore it is now possible to express T_C and χ_M^{-1} as a function of the lattice constant a only:

$$\chi_M^{-1}(a) = \frac{1}{C_0}\left[T - T_{C,0}\left(1 + [K_v + K_d\gamma^2\Theta(\tilde{a}-a)]\frac{a-\tilde{a}}{\tilde{a}}\right)\right], \tag{19}$$

where $K_v = 2K_a + K_c = 8.8$. This equation shows that if the lattice expands strongly with temperature, χ_M^{-1} decreases.

For temperatures between T_p and about 390 K, as well as above T_s, a increases approximately linearly with temperature (see Fig. 5) and can therefore be written as

$$a(T) = a(T_0)\left[1 + \alpha\frac{T-T_0}{T_0}\right], \tag{20}$$

where the experimental values for the coefficients are $T_{0,+} = T_s = 452$ K, $a(T_s) = \tilde{a} = 3.699$ Å, and $\alpha_+ = 0.0126$ for temperatures above T_s (the index + denotes the high-temperature region above T_s) and $T_{0,-} = T_p = 318$ K, $a(T_p) = 3.673$ and $\alpha_- = 0.0284$ for temperatures between T_p and about 390 K (the index "−" denotes the intermediate temperature region). By inserting Eq. (20) into Eq. (19) we obtain for the high-temperature region above T_s:

$$\chi_M^{-1}(T) = \frac{1}{C_{eff}}(T - T_{C,eff}), \tag{21}$$

with

$$C_{eff} = \frac{1}{1 - K_v\alpha_+\frac{T_{C,0}}{T_s}}C_0,$$

$$T_{C,eff} = \frac{1 + K_v\alpha_+}{1 - K_v\alpha_+\frac{T_{C,0}}{T_s}}T_{C,0}. \tag{22}$$

$T_{C,eff}$ and C_{eff} are the experimentally accessible quantities for the high-temperature susceptibility, and due to the expansion of the lattice, they are different from $T_{C,0}$ and C_0. The experimentally measured values are $T_{C,eff} = 285$ K and $C_{eff} = 3.12 \times 10^{-5}$ m^3 K,[14] which corresponds to an effective magnetic moment of $3.57\mu_B$. From C_{eff} and $T_{C,eff}$ the values of $T_{C,0} = T_C(\tilde{a})$ and C_0 can now be obtained:

$$C_0 = \frac{1 - K_v\alpha_+}{1 - K_v\alpha_+\left(1 - \frac{T_{C,eff}}{T_s}\right)}C_{eff},$$

$$T_{C,0} = \frac{1}{1 - K_v\alpha_+\left(1 - \frac{T_{C,eff}}{T_s}\right)}T_{C,eff}. \tag{23}$$

All the variables on the right-hand side of Eq. (23) can be obtained from experiments except K_v. For small K_v the difference between $T_{C,0}$ and $T_{C,eff}$ is proportional to K_v. Since T_s is larger than the experimental value of $T_{C,eff}$, the effect of the thermal expansion of the hexagonal structure is a reduction of the slope of the inverse susceptibility as a function of temperature, as well as a reduction of the extrapolated Curie temperature as compared to the real Curie temperature.

In the region where linear expansion holds the slope of the inverse susceptibility above T_t is

$$\frac{\partial\chi_{M,+}^{-1}}{\partial T} = \frac{1}{C_0}\left(1 - K_v\alpha_+\frac{T_{C,0}}{T_t}\right), \tag{24}$$

whereas for in the intermediate temperature region above T_p it is

$$\frac{\partial\chi_{M,-}^{-1}}{\partial T} = \frac{1}{C_0}\left(1 - (K_v + K_d\gamma^2)\alpha_-\frac{a_0}{\tilde{a}}\frac{T_{C,0}}{T_{0,-}}\right). \tag{25}$$

In both regions there is a reduction of the slope due to the expansion of the lattice. However, the reduction is much larger for $\chi_{M,-}$ than for $\chi_{M,+}$, since there is the additional term proportional to K_d due to the distortion and also $\alpha_- > \alpha_+$. As a rough approximation it can be assumed that $(a_0 T_{C,0})/(\tilde{a}T_{0,-}) \approx 1$, so that $\frac{\partial\chi_{M,-}^{-1}}{\partial T}$ becomes negative for

$$(K_v + K_d\gamma^2)\alpha_- > 1. \tag{26}$$

The values of α_- and γ are determined experimentally and describe how the structure changes with temperature, whereas K_v and K_d describe how T_C varies for distorted cells. By using our calculated values for K_v and K_d we obtain $(K_v + K_d\gamma^2)\alpha_- = 1.29$. This is indeed larger than 1. Therefore we do predict a negative slope for the inverse susceptibility in the intermediate-temperature region. With the value for $\gamma=947$ estimated in Sec. III D we obtain $(K_v + K_d\gamma^2)\alpha_- = 0.92$, which is still smaller than 1. This is due to the underestimation of the distortion as compared to experiments by using $\gamma=947$. With $\gamma=1186$ the reduction of the distortion with increasing lattice constant is large enough to obtain a negative slope of the inverse susceptibility, whereas $\gamma=947$ underestimates the reduction of the distortion, and so the slope of the inverse susceptibility is reduced but not to the point to make it negative.

Finally we will extract the values for K_v and K_d from the experimental behavior of the Curie temperature. Since the ratio between K_a and K_c cannot be obtained from the thermal properties of MnAs, it is therefore assumed that $K_c/K_a = -1/4.9 \simeq -0.2$ is fixed and corresponds to our calculated value. For the hexagonal cell ($d=0$), Eq. (17) reads

$$T_C(a,c) = T_{C,0}\left[1 + K_v\left(k_a\frac{a-\tilde{a}}{\tilde{a}} + k_c\frac{c-\tilde{c}}{\tilde{c}}\right)\right], \tag{27}$$

where $k_a = 2/(2 + K_c/K_a) = 1.11$ and $k_c = (K_c/K_a)/(2 + K_c/K_a) = -0.11$. This has to be valid for all temperatures where the

TABLE II. Main parameters used in the description of the phase diagram of MnAs. We compared results obtained from *ab initio* calculations and Heisenberg model (DFT), with those of the best fit of the experimental properties (FIT).

	$T_{C,0}$ (K)	K_d (10^{-5})	K_v	K_a	K_c	γ	$\tilde{a}$ (Å)
DFT	579	2.62	8.8	4.9	−1.0	947	3.706
FIT	311	1.78	18.1	10.1	−2.1	1184	3.699

cell is hexagonal; therefore, it cannot be assumed that the ratio between c and a is constant since it changes abruptly from 1.533 to 1.556 at T_p. By using the expression for $T_{C,0}$ from Eq. (23) we obtain K_v:

$$K_v = \frac{\frac{T_C(a,c)}{T_{C,\mathrm{eff}}} - 1}{\alpha_+\left(\frac{T_C(a,c)}{T_{C,\mathrm{eff}}} - \frac{T_C(a,c)}{T_s}\right) + k_a\frac{a-\tilde{a}}{\tilde{a}} + k_c\frac{c-\tilde{c}}{\tilde{c}}}. \quad (28)$$

As reference Curie temperature the extrapolated value to room temperature is used, which can be estimated to be about $T_C(a=3.724\ \text{Å}, c=1.533a)=360$ K. By inserting the experimental values for the parameters on the right-hand side of Eq. (28) we obtain $K_v=18.1$. This is about twice as big as our predicted value. The disagreement may partly be due to the fact that the ratio between K_c and K_a has been fixed for our calculated value. By inserting this value for K_v in Eq. (23) we obtain $T_{C,0}=311$ K, the Curie temperature for the lattice parameters at $T=T_s$.

In order to extract K_d from experiments we use the relative change in the slope of the inverse susceptibility around T_t. This is, according to Eqs. (24) and (25),

$$\frac{\frac{\partial\chi^{-1}_{M,+}}{\partial T} - \frac{\partial\chi^{-1}_{M,-}}{\partial T}}{\frac{\partial\chi^{-1}_{M,+}}{\partial T}} = 1 - \frac{1-(K_v+K_d\gamma^2)\alpha_-\frac{a_0}{\tilde{a}}\frac{T_{C,0}}{T_0}}{1-K_v\alpha_+\frac{T_{C,0}}{T_t}}, \quad (29)$$

and increases with increasing K_v and K_d. All the variables in this equation can be derived from the experimental measurements, except K_v and K_d. Experimentally different values are found for the relative change of the slope [left-hand side of Eq. (29)].[24,55–57] These are all of the order of 1.44. By using this value for the relative change of the slope and the previously calculated value $K_v=18.1$, K_d is found to be 1.78×10^{-5}. This value agrees approximately with our predicted value of 2.62×10^{-5}.

In conclusion, Table II summarizes the parameters calculated in this article, by comparing our *ab initio* results obtained from the DFT calculations and the Heisenberg model, with the results obtained by fitting to the experimental data. In general the value obtained from the *ab initio* calculations agrees with the best fit to experiments, although the DFT results underestimate K_v and overestimate K_d.

V. CONCLUSIONS

We have investigated, by means of *ab initio* electronic structure calculations, the magnetostructural properties of MnAs. The stable structure for the ferromagnetic state is found to be the $B8_1$ structure. However, if antiferromagnetic alignment in the hexagonal plane is imposed, the $B31$ structure becomes more stable. By fitting the DFT total energies of different magnetic configurations to a Heisenberg-type energy it is shown that the main contributions to the physical properties originate from the exchange coupling parameters up to the third nearest neighbor. The Curie temperature was calculated in the mean-field approximation, with values approximately twice as large as the experimental ones.

The main assumption of the phenomenological model of Bean and Rodbell[11] that the ferromagnetic exchange coupling parameters increase when the volume is increased has been confirmed [Eq. (16)] using this analysis. However, it has been shown that the exchange interactions depend not only on the volume, but that the orthogonal distortion to the $B31$ structure plays an important role. For the experimentally observed distortions some of the in-plane exchange coupling coefficients become antiferromagnetic. This is the reason for the stability of the $B31$ structure for those configurations of the magnetic moments that have an antiferromagnetic component in the hexagonal plane.

Furthermore, it has been shown that for paramagnetic states the $B31$ structure is stable at small volumes, while the $B8_1$ structure is stable above a critical lattice constant of about 3.7 Å. This explains the second-order phase transition at T_t, since at that temperature the lattice constant crosses this critical value.

The Curie temperature has been expanded as a function of the lattice vectors and of the amount of distortion. An increase in the volume leads to an enhancement of the Curie temperature, while an increase of the distortion leads to a reduction. With these results in hand the increase of the susceptibility between T_p and T_t has been explained as the result of the increase of the Curie temperature due to the change of the structure from $B31$ to $B8_1$ and to the increase of the volume. By using the experimental variation of the lattice parameters with rising temperature the susceptibility is

indeed found to increase between T_p and T_t.

A fit of the dependence of the Curie temperature on the lattice parameters to best reproduce the experimental behavior is also given. The calculated values agree within a factor of 2 with the values obtained from *ab initio* calculations. Our results are in agreement with the various phenomenological models based on the Bean-Rodbell idea. In this work the various parameters used in those models for the magnetostructural properties of MnAs have been derived from first principles and therefore validated.

ACKNOWLEDGMENTS

We acknowledge financial support from SFI (Grant No. SFI02/IN1/I175). Computational resources have been provided by the HEA IITAC project with support of the Trinity Centre for High Performance Computing and by ICHEC.

[1] A. K. Das, C. Pampuch, A. Ney, T. Hesjedal, L. Däweritz, R. Koch, and K. H. Ploog, Phys. Rev. Lett. **91**, 087203 (2003).
[2] K. Akeura, M. Tanaka, M. Ueki, and T. Nishinaga, Appl. Phys. Lett. **67**, 3349 (1995).
[3] K. H. Ploog, Physica E (Amsterdam) **24**, 101 (2004).
[4] J. H. Song, J. J. Lee, Y. Cui, J. B. Ketterson, and S. Cho, Appl. Phys. Lett. **85**, 4079 (2004).
[5] J. H. Song, Y. Cui, J. J. Lee, Y. Kim, J. B. Ketterson, and S. Cho, J. Appl. Phys. **95**, 7288 (2004).
[6] M. Ramsteiner, H. Y. Hao, A. Kawaharazuka, H. J. Zhu, M. Kästner, R. Hey, L. Däweritz, H. T. Grahn, and K. H. Ploog, Phys. Rev. B **66**, 081304(R) (2002).
[7] M. J. S. P. Iikawa, F. Brasil, O. D. D. Couto, C. Adriano, C. Giles, and L. Däweritz, Appl. Phys. Lett. **85**, 2250 (2004).
[8] F. Iikawa, M. J. S. P. Brasil, C. Adriano, O. D. D. Couto, C. Giles, P. V. Santos, L. Däweritz, I. Rungger, and S. Sanvito, Phys. Rev. Lett. **95**, 077203 (2005).
[9] J. Mira, F. Rivadulla, J. Rivas, A. Fondado, T. Guidi, R. Caciuffo, F. Carsughi, P. G. Radaellil, and J. B. Goodenough, Phys. Rev. Lett. **90**, 097203 (2003).
[10] T. Suzuki and H. Ido, J. Phys. Soc. Jpn. **51**, 3149 (1982).
[11] C. P. Bean and D. S. Rodbell, Phys. Rev. **126**, 104 (1962).
[12] R. W. De Blois and D. S. Rodbell, Phys. Rev. **130**, 1347 (1963).
[13] J. B. Goodenough and J. A. Kafalas, Phys. Rev. **157**, 389 (1967).
[14] N. Menyuk, J. A. Kafalas, K. Dwight, and J. B. Goodenough, Phys. Rev. **177**, 942 (1969).
[15] F. Groønvold, S. Snildal, and E. F. Westrum, Jr., Acta Chem. Scand. (1947-1973) **24**, 285 (1970).
[16] A. Zieba, K. Selte, A. Kjekshus, and A. F. Andresen, Acta Chem. Scand., Ser. A **32**, 173 (1978).
[17] A. Zieba, Y. Shapira, and S. Foner, Phys. Lett. **91A**, 243 (1982).
[18] V. A. Chernenko, L. Wee, P. G. McCormick, and R. Street, J. Appl. Phys. **85**, 7833 (1999).
[19] F. Ishikawa, K. Koyama, K. Watanabe, and H. Wada, Jpn. J. Appl. Phys., Part 2 **42**, L918 (2003).
[20] J. B. Forsyth, S. J. Pickart, and P. J. Brown, Proc. Phys. Soc. London **88**, 333 (1966).
[21] R. Koch, C. Pampuch, H. Yamaguchi, A. K. Das, A. Ney, L. Däweritz, and K. H. Ploog, Phys. Rev. B **70**, 092406 (2004).
[22] B. T. M. Willis and H. P. Rooksby, Proc. Phys. Soc. London, Sect. B **67**, 290 (1954).
[23] R. H. Wilson and J. S. Kasper, Acta Crystallogr. **17**, 95 (1964).
[24] L. Pytlik and A. Zieba, J. Magn. Magn. Mater. **51**, 199 (1985).
[25] C. Kittel, Phys. Rev. **120**, 335 (1960).
[26] D. S. Rodbell and C. P. Bean, J. Appl. Phys. **33**, 1037 (1962).
[27] K. Bärner, E. A. Zavadskii, and D. Y. Suminov, Phys. Status Solidi B **214**, 411 (1999).
[28] L. H. Schwartz, E. L. Hall, and G. P. Felcher, J. Appl. Phys. **42**, 1621 (1971).
[29] S. Haneda, N. Kazama, Y. Yamaguchi, and H. Watanabe, J. Phys. Soc. Jpn. **42**, 31 (1977).
[30] S. Haneda, N. Kazama, Y. Yamaguchi, and H. Watanabe, J. Phys. Soc. Jpn. **42**, 1212 (1977).
[31] T. Kato, K. Nagai, and T. Aisaka, J. Phys. C **16**, 3183 (1983).
[32] I. M. Vitebskii, V. I. Kamenev, and D. A. Yablonskii, Sov. Phys. Solid State **23**, 121 (1981).
[33] S. K. Asadov, E. A. Zavadskii, V. I. Kamenev, E. P. Stefanovskii, A. L. Sukstanskii, and B. M. Todris, Phys. Solid State **42**, 1696 (2000).
[34] V. I. Val'kov and A. V. Golovchan, Low Temp. Phys. **30**, 711 (2004).
[35] K. Motizuki and K. Katoh, J. Magn. Magn. Mater. **54-57**, 1097 (1986).
[36] K. Motizuki, J. Magn. Magn. Mater. **70**, 1 (1987).
[37] R. Podloucky, J. Magn. Magn. Mater. **43**, 204 (1984).
[38] R. Podloucky, J. Phys. F: Met. Phys. **14**, L145 (1984).
[39] S. Sanvito and N. A. Hill, Phys. Rev. B **62**, 15553 (2000).
[40] P. Ravindran, A. Delin, P. James, B. Johansson, J. M. Wills, R. Ahuja, and O. Eriksson, Phys. Rev. B **59**, 15680 (1999).
[41] A. Continenza, S. Picozzi, W. T. Geng, and A. J. Freeman, Phys. Rev. B **64**, 085204 (2001).
[42] Y.-J. Zhao, W. T. Geng, A. J. Freeman, and B. Delley, Phys. Rev. B **65**, 113202 (2002).
[43] R. de Paiva, J. L. A. Alves, R. A. Nogueira, J. R. Leite, and L. M. R. Scolfaro, Braz. J. Phys. **34**, 568 (2004).
[44] A. Debernardi, M. Peressi, and A. Baldereschi, Comput. Mater. Sci. **27**, 175 (2003).
[45] A. Debernardi, M. Peressi, and A. Baldereschi, Mater. Sci. Eng., C **23**, 1059 (2003).
[46] M. Shirai and Y. Tokioka, J. Electron Spectrosc. Relat. Phenom. **88-91**, 357 (1998).
[47] K. Motizuki, K. Katoh, and A. Yanase, J. Phys. C **19**, 495 (1986).
[48] M. K. Niranjan, B. R. Sahu, and L. Kleinman, Phys. Rev. B **70**, 180406(R) (2004).
[49] V. I. Valkov and A. V. Golovchan, Low Temp. Phys. **31**, 528 (2005).
[50] J. M. Soler, E. Artacho, J. D. Gale, A. Garcia, J. Junquera, P. Ordejon, and D. Sanchez-Portal, J. Phys.: Condens. Matter **14**, 2745 (2002).
[51] J. P. Perdew, K. Burke, and M. Ernzerhof, Phys. Rev. Lett. **77**, 3865 (1996).
[52] T. Asada and K. Terakura, Phys. Rev. B **47**, 15992 (1993).

[53] R. S. Mulliken, J. Chem. Phys. **23**, 1833 (1955).
[54] M. Pajda, J. Kudrnovsky, I. Turek, V. Drchal, and P. Bruno, Phys. Rev. B **64**, 174402 (2001).
[55] C. Guillaud, J. Phys. Radium **12**, 223 (1951).
[56] Z. S. Basinski, R. O. Kornelsen, and W. B. Pearson, Trans. Indian Inst. Met. **13**, 143 (1960).
[57] K. Selte, A. Kjekshus, and A. F. Andresen, Acta Chem. Scand., Ser. A **28**, 61 (1974).